Transient Catenation in a Zirconium-Based Metal–Organic Framework and Its Effect on Mechanical Stability and Sorption Properties

Lee Robison, Xinyi Gong, Austin M Evans, Florencia A Son, Xingjie Wang, Louis R Redfern, Megan C Wasson, Zoha H Syed, Zhijie Chen, Karam B Idrees, et al.

Transient Catenation in a Zirconium-Based Metal-Organic Framework and its Effect on Mechanical Stability and Sorption Properties

Lee Robison,[†,‡,#] Xinyi Gong,[†,‡,#] Austin M. Evans,[†] Florencia A. Son,[†] Xingjie Wang,[†] Louis R. Redfern,[†] Megan C. Wasson,[†] Zoha H. Syed,[†∥] Zhijie Chen,[†] Karam B. Idrees,[†] Timur Islamoglu,[‡] Massimiliano Delferro,[∥] William R. Dichtel, [†] François-Xavier Coudert,[§] Nathan C. Gianneschi, [*†,‡,⊥] Omar K. Farha,[*,†,‡,Ω]

[†]Department of Chemistry, Northwestern University, 2145 Sheridan Road, Evanston, IL 60208, USA

[‡]International Institute of Nanotechnology, Department of Chemistry, Northwestern University, Evanston, Illinois 60208, USA

[Ω]Department of Chemical and Biological Engineering, Northwestern University, 2145 Sheridan Road, Evanston, IL 60208, USA

[§]Chimie ParisTech, PSL University, CNRS, Institut de Recherche de Chimie Paris, 75005 Paris, France

[⊥]Department of Biomedical Engineering, Department of Materials Science & Engineering, Department of Pharmacology, Simpson-Querrey Institute, Chemistry of Life Processes Institute, Lurie Cancer Center, Northwestern University, 2145 Sheridan Road, Evanston, Illinois 60208, USA

[∥]Chemical Sciences and Engineering Division, Argonne National Laboratory, Lemont, Illinois 60439, USA.

KEYWORDS: metal–organic frameworks, catenation, transmission electron microscopy**,** mechanical properties

ABSTRACT

Interpenetration of two or more sublattices is common among many metal–organic frameworks (MOFs). However, interpenetration in zirconium cluster-based MOFs is rarely observed. Herein, we study the evolution of one zirconium cluster-based, 3,8-connected MOF from its non-interpenetrated (NU-1200) to interpenetrated (STA-26) isomer. We observe this transient catenation process indirectly using ensemble methods, such as nitrogen porosimetry and X-ray diffraction, and directly, using high-resolution transmission electron microscopy. The approach detailed here will serve as a template for other researchers to monitor the interpenetration of their MOF samples at the bulk and single-particle limits. We investigate the mechanical stability of both lattices experimentally by pressurized *in situ* X-ray diffraction and nanoindentation as well as computationally with density functional theory (DFT) calculations. Both lines of study reveal that STA-26 is considerably more mechanically stable than NU-1200. We conclude this study by demonstrating the potential of these MOFs and their mixed phases for the capture of gaseous *n*-hexane, used as a structural mimic for the chemical warfare agent, sulfur mustard gas.

INTRODUCTION

Metal–organic frameworks (MOFs) are hybrid materials obtained by the self-assembly of inorganic nodes and organic linkers into periodic multidimensional structures with high surface areas and porosities.[1, 2] Among the thousands of MOFs synthesized to-date, zirconium cluster-based MOFs are particularly robust due to the strength of the Zr(IV)-carboxylate bond.[3-5] As such, Zr-based MOFs have been explored for applications that may require demanding conditions such as catalysis,[6, 7] water sorption,[8-10] and gas separations.[11, 12]

Interpenetration is defined by the presence of two or more mechanically interlocked periodic networks where, although no chemical bonds exist between the frameworks, disentanglement can only be achieved by breaking chemical bonds (**Fig. 1**).[13] Interpenetration typically enhances the stability of a supramolecular framework by filling void space, which increases the density and the abundance of repulsive forces that prevent framework collapse.[14] These attributes of interlocked networks increase the mechanical strength of the material,[15] although they decrease the surface area and porosity of the structures as compared to their noninterpenetrated counterparts. Nevertheless, many interpenetrated MOFs exhibit excellent gas separation and selectivity characteristics due to their tunable pore sizes.[16, 17,18] In addition to the interpenetrated Zr-based MOF investigated in this study, other interpenetrated Zr-based MOFs have been reported.[19-22] Among these, the UiO-66 type interpenetrated MOFs have been well known.[23-29] Other systems which exhibit interpenetration were found during isoreticular expansion of the linkers and have either ditopic[30-34] or tetratopic linkers,[35-38] which makes the relatively short tritopic linker used in this study a unique case. Herein, we explore the transient catenation processes between two different interpenetrations of a 3,8-connected Zr-based MOF, known as NU-1200 and STA-26 in its non-interpenetrated and interpenetrated forms, respectively.

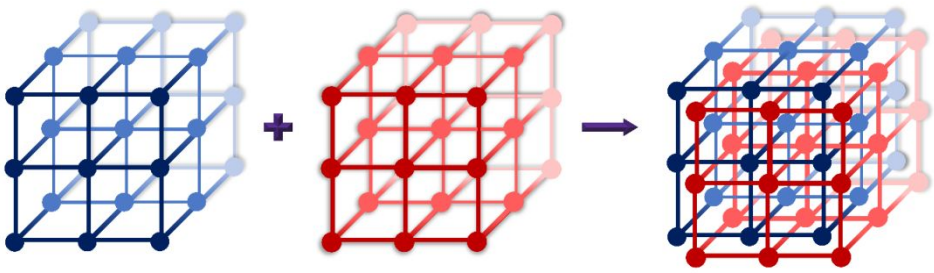

Figure 1. Schematic of non-interpenetrated frameworks and the doubly interpenetrated analogue.

Contemporary framework interpenetration studies rely heavily on bulk characterization techniques.[18] However, investigations into catenation processes via direct imaging at the single-particle limit have not yet been performed. While single-crystal X-ray diffraction (SCXRD) can be used to study single particles, the indirectly obtained structure is extracted from the average positions of atoms in a crystal. This can become challenging to interpret when positional or substitutional disorder is present. Furthermore, single-crystal X-ray diffraction evaluates individual particles, which may not be representative of the bulk. In this work, we examine the zirconium cluster-based non-interpenetrated NU-1200 MOF and the analogous doubly interpenetrated STA-26 MOF at the single particle level using high-resolution transmission electron microscopy (TEM) coupled with an automated post-processing script that analyzes interpenetration across many images. These single-particle studies are complemented by ensemble characterization techniques such as powder X-ray diffraction (PXRD) and adsorption isotherms with several probe molecules, including a structural mimic for a chemical warfare agent. These investigations reveal that catenation occurs in a near stepwise process within individual particles, which leads to mixtures of pure phases of the interpenetrated and non-interpenetrated structures rather than partially catenated particles. This observation led us to study the thermodynamics and mechanical properties of both pure phases via density functional theory (DFT), *in situ* synchrotron X-ray diffraction, and nanoindentation experiments. Collectively, these studies enable the reliable characterization of two different interpenetrated and non-interpenetrated Zr-based MOFs and reveal their promise for applications where demanding mechanical stresses are encountered, including the storage of toxic chemical warfare agents.[39, 40]

RESULTS and DISCUSSION

Herein, we characterize the properties of two distinct zirconium cluster-based, 3,8-connected MOFs (**Fig. 2A**). Each MOF features 4,4′,4″-(2,4,6-trimethylbenzene-1,3,5-triyl)tribenzoic acid (TMTB) linkers and $Zr_6(\mu_3\text{-}OH)_4(\mu_3\text{-}O)_4(OH)_4(OH_2)_4$ Zr_6-oxo cluster metal nodes. The tritopic TMTB linkers and 8-connected Zr_6-oxo clusters assemble to form the non-interpenetrated NU-1200, which possesses 14Å diameter sodalite cages and mesoporous 1D channels that are 20 Å in width. The NU-1200 MOF features the topology (cubic clusters and triangular ligands) and crystallizes in the $Pm\bar{3}m$ space group.[41, 42] Additional characterization data is available in SI (**Fig. S1-S3**).

Wright, Prasad, and co-workers reported that the same TMTB linker and Zr_6-oxo cluster metal node produces STA-26, a doubly interpenetrated analogue of NU-1200.[43] The authors synthetically targeted the structure by changing the identity and concentration of the modulating species present during the synthesis. The STA-26 MOF possesses the same the topology but is microporous rather than mesoporous as a result of the second lattice being displaced by $[\frac{1}{2}\frac{1}{2}\frac{1}{2}]$ from the original non-interpenetrated NU-1200 framework. This displacement means that the vertex of one sublattice is in the exact center of the sodalite cages of the other, while the diameter of the octahedral cages remains the same (14Å). The STA-26 MOF exhibits $Im\bar{3}m$ symmetry.

However, we observed that the interpenetration can be initiated post-synthetically, and the degree of interpenetration between these two networks could be controlled by regulating the reaction time. We initiated the interpenetration of NU-1200 to STA-26 by exposing 20 mg of thermally activated NU-1200 to a solution of DMF:HCOOH that is 2.5:1 by volume at 120 °C for 40, 110 or 180 min, and referred as NU-1200-x or STA-26-x where x indicates the time that MOF particles spend in DMF:HCOOH solution. We found that this transient catenation process was complete after 110 min. We monitored this transition using PXRD (Cu Kα1 radiation, λ = 1.54056 Å) by tracking the disappearance of the peak at 2θ = 3.1°, which corresponds to the NU-1200 (100) Bragg feature, and the growth of the 4.42° feature, which corresponds to the (110) reflection of STA-26 **(Fig. 2B).** We posit a mechanism for this process, but it is preliminary as we do not have comprehensive experimental data to explain the process.[44] Nitrogen isotherms obtained along the course of this transition demonstrated a decrease in gravimetric adsorption capacity consistent with the interpenetrated framework decreasing the total void space of the MOF. Similarly, the extracted pore sizes calculated from the nonlocal density functional theory (NLDFT) model for Pillared Clay reveal that during this transition the mesopore of NU-1200 (20 Å) disappears, and after 110 min of soaking in formic acid/DMF solution, only the STA-26 micropore (10 Å) is observed. To determine if the phase transition to the denser STA-26 interpenetrated phase could be reversed to the mesoporous NU-1200, which could imply entropic control between the two, we applied the original synthesis conditions to activated STA-26. However, we found that we could not reverse the interpenetration trend we observe (**Fig S4**).

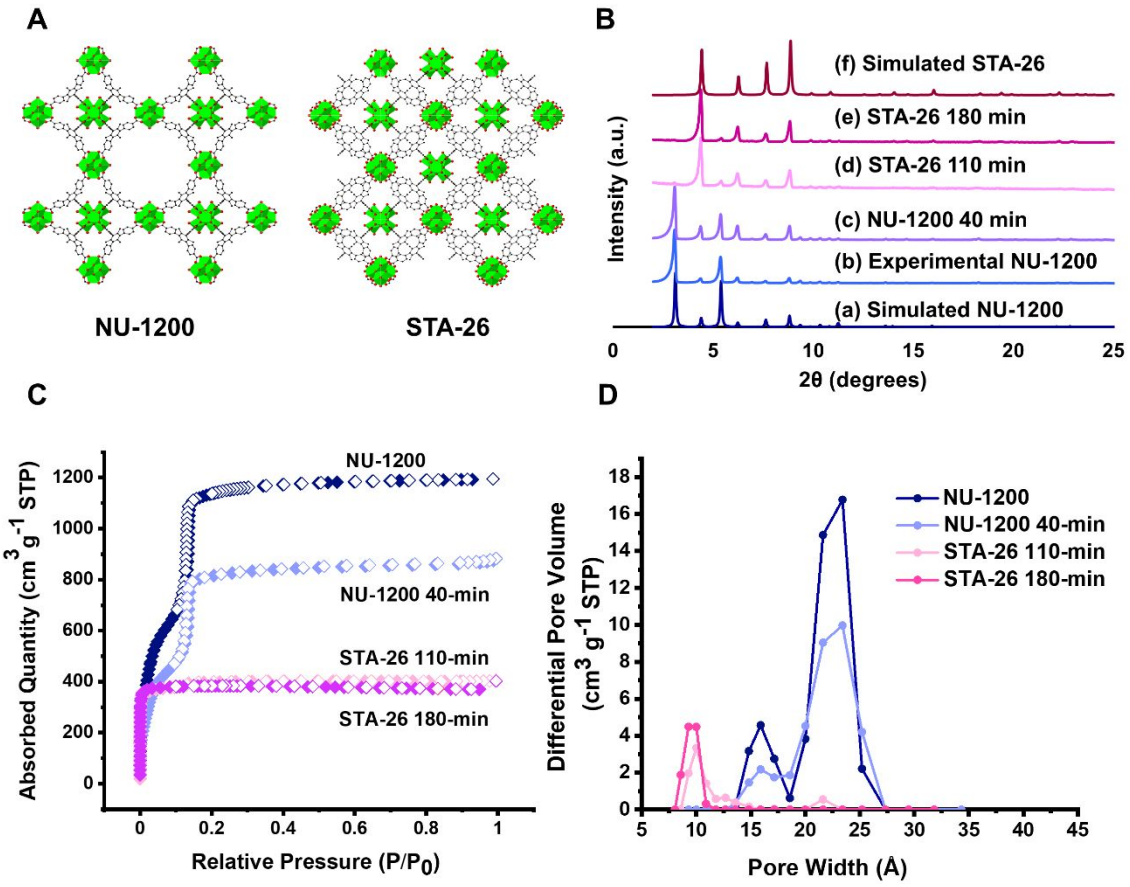

Figure 2. (**A**) NU-1200 and its interpenetrated analogue STA-26. (**B**) PXRD patterns of non-interpenetrated NU-1200 transiently transforming to interpenetrated STA-26 over variable reaction times. (**C**) Nitrogen sorption isotherms and (**D**) NLDFT-calculated pore size distributions of NU-1200 crystals transforming to STA-26 crystals over variable reaction times.

TEM Imaging and Automated Interpenetration Mapping

Despite the numerous investigations into framework catenation processes,[18] there still exists a limited understanding of how this process occurs within single particles. Recently, high-resolution transmission electron microscopy (HR-TEM) hardware and imaging techniques have been developed to study beam-sensitive materials, such as MOFs.[45] Here, we combine those advances with an automated post-processing Fourier transform mapping technique to explore the transition of NU-1200 to STA-26 at the single-particle limit (**Fig 3**). We first imaged samples of the non-interpenetrated NU-1200 and interpenetrated STA-26. Fast Fourier transforms (FFTs) of MOF particles on the [100] zone axis showed the expected lattice symmetries of $Pm\bar{3}m$ and $Im\bar{3}m$ for NU-1200 and STA-26, respectively (**Fig. S5**). Due to this difference in symmetry, and accompanying difference in electron density contrast, these two lattices can be resolved by

evaluating the relative intensity ratios of the FFT features at 0.36 nm^{-1} and 0.49 nm^{-1} that correspond to real spacings of 2.8 nm and 2.0 nm, respectively. Using this understanding, we developed a post-processing script, which automatically rasters a small region-of-interest across an image, extracts the Fourier transform of that sub-image, and then assigns the dominant interpenetration within that region based on the relative intensity ratios of the FFT features mentioned above (**Fig. S6**). This method allows us to spatially resolve the interpenetration of entire crystallites across a series of images. When this method was applied to pure crystal phases, we found that the script could reliably disambiguate the two phases (**Fig. S7-S8**).

We then applied the same technique to microtome-cut intermediate timepoint samples, NU-1200 40 min and STA-26 110 min, which we obtained along the course of the interpenetration transition. This approach allows us to statistically investigate the process of transient catenation. In particular, we investigated whether interpenetration occurs gradually across all crystals within a sample or whether two predominantly pure phases are present at all times, which would be challenging to resolve using bulk techniques such as powder X-ray diffraction or nitrogen adsorption at 77 K.

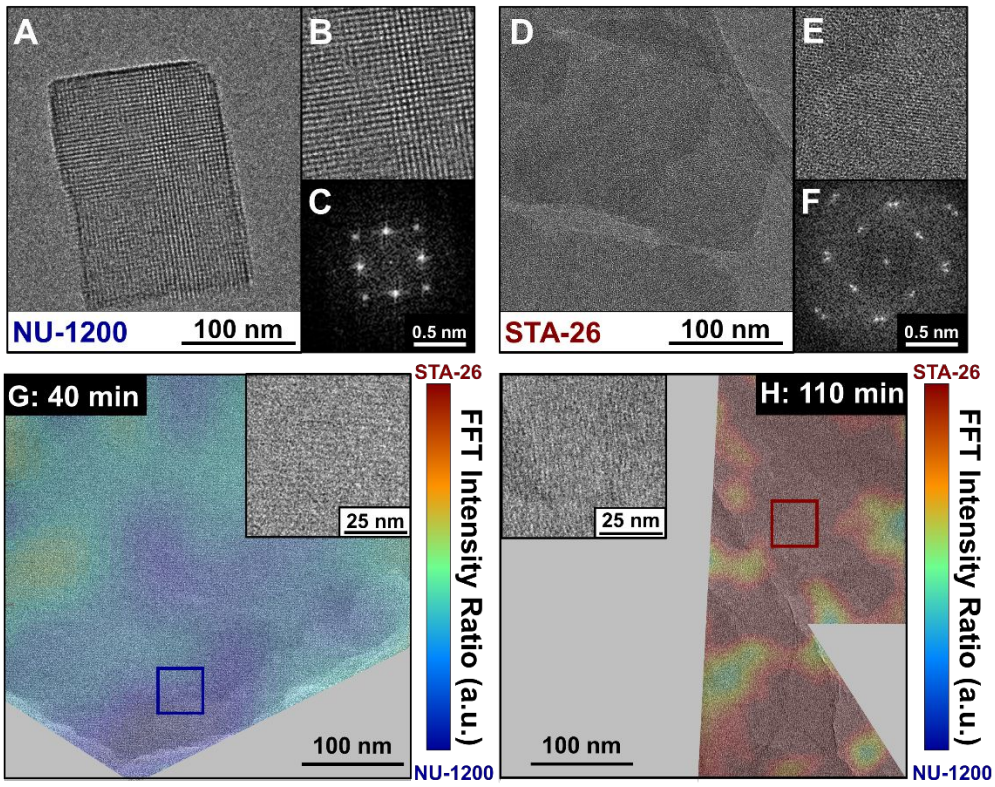

Figure 3. High-resolution transmission electron micrographs of pure-phase (**A-B**) NU-1200 and (**D-E**) STA-26. Fourier transforms of (**C**) NU-1200 and (**F**) STA-26. (**G**) Transmission electron micrograph obtained after 40 min of reaction revealing a predominant non-interpenetrated structure. Lattice-resolution image of the blue boxed region in **G**, showing a NU-1200 structure. (**H**) Transmission electron micrograph obtained after 110 min of reaction revealing a predominant interpenetrated structure. Lattice-resolution image of the red boxed region in **G**, showing an STA-26 structure. Grey regions indicate void space, lacey carbon substrate, or damaged crystallites.

From our post-imaging analysis, we predominantly observed that pure phases were present at all times, which suggests that once an interpenetration transition is initialized it occurs rapidly and completely. Across several images of NU-1200 40 min (**Fig. S9-S10**), we found that nearly all particles were obtained as pure non-interpenetrated NU-1200 (**Fig. S13**). However, a select number of particles were obtained as the pure STA-26 phase. In contrast, we found the images of the STA-26 110 min sample (**Fig. S11-S12**) dominated by the interpenetrated STA-26 crystallites (**Fig. S14**). In rare instances, we observed minor, residual NU-1200 non-interpenetrated domains at the fringes of these crystallites (**Fig. S15-S18**), which may account for the minor X-ray diffraction features observed at prolonged reaction times. The non-interpenetrated lattice being confined at the edge of these intermixed particles indicates that edges are the final location to interpenetrate. Taken together, these results suggest that catenation occurs rapidly from NU-1200 to STA-26 within single particles. This contrasts with the possibility that the catenation process occurs gradually across all crystallites, which would lead to the prevalent observation of intermixed phases within single particles. This finding has implications for the physical properties of samples undergoing catenation, which in this case are likely to behave similarly to physical mixtures of pure phases. More investigation is needed to resolve the thermodynamic and kinetic underpinnings of this transition.

Physical Mixtures of Multiple Phases

From our findings that intermediate samples were predominantly single-phase particles, we decided to compare our ensemble measurements performed on intermediate samples with those of physical mixtures of pure NU-1200 and pure STA-26 phases. We observed the same decrease in nitrogen sorption capacity, reduction in the differential pore volume and pore size, and change in PXRD pattern for the physical mixtures (**Fig. S19**) as MOF samples measured during the interpenetration process (**Fig. 2**).

Our ensemble and direct imaging findings lead us to conclude that the interpenetration of NU-1200 occurs very quickly, with some percentage of crystals in intermediate samples being doubly interpenetrated STA-26 or non-interpenetrated NU-1200. This contrasts with our initial hypothesis that we synthesized MOFs exhibiting partial interpenetration. Combined with our TEM mapping results, we conclude that the decrease in adsorbed nitrogen and concurrent decrease in pore volume dominantly arises from different ratios of the two phases. The total uptake of N_2 from the nitrogen sorption isotherms of the physical mixtures (**Fig. S19)** display a linear relationship ($R^2 = 0.96$) from non-interpenetrated to doubly interpenetrated (**Fig. S20**). Additionally, we observed a linear relationship ($R^2 = 0.96$) between the total pore volume (cc g^{-1}) plotted and the ratio of pure crystals that are mixed (**Fig. S21**). These observations are largely consistent with our observation of a stepwise transition from the NU-1200 to the STA-26 phase, rather than gradual framework interpenetration within single particles.

Reinforced Mechanical Strength of Interpenetrated Lattices

Previous work in the MOF field has established interesting pressure-induced behavior in framework materials, including discovery of new phases, polymorphism, negative linear compressibility and single crystal to single crystal phase transitions, among others.[46-50] While it is generally understood that physical properties of MOFs are affected by interpenetration, very few studies have explored the differences between mechanical strength of differentially interpenetrated chemically identical networks.[15] To our knowledge this is the first study to combine DFT computations and experimental work to determine the effect of interpenetration on the hydrostatic, uniaxial, and shear stress on a MOF structure. Studying the bulk mechanical properties of differently interpenetrated structures[51] is crucial for the use of MOFs in commercial applications which require that powdered MOF samples be processed into shaped constructs such as pellets, extrudates, or as composite materials.[52-54]

We investigated NU-1200 and STA-26 using density functional theory (DFT) to obtain values for the bulk modulus (*K*), the Young's modulus (*E*), and the shear modulus (*G*) (**Fig. 4**).[55] Each structural model behaved well under energy minimization, with lattice parameters in good agreement with the experimentally obtained crystal structures. The interpenetrated STA-26 structure is 223 kJ mol^{-1} more stable than the non-interpenetrated NU-1200 framework. This value

agrees with other large-pore interpenetrated frameworks[15] and reveals that the non-interpenetrated phase is metastable compared to its denser interpenetrated analogue (see supporting information for additional computational details). This finding is in line with other additional classes of porous materials (mesoporous silicas and siliceous zeolites)[56, 57] along with other MOF frameworks.[58, 59]

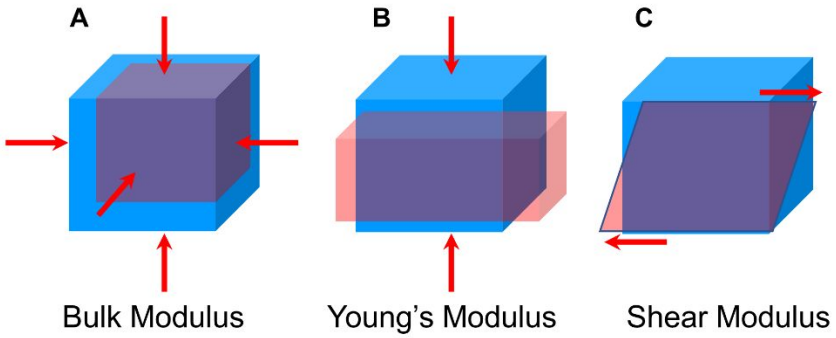

MOF	Bulk modulus (*K*)	Young's modulus (*E*)	Shear modulus (*G*)
NU-1200	8.1 GPa	2.3 GPa	0.8 GPa
STA-26	15.1 GPa	3.8 GPa	1.3 GPa

Figure 4. Illustrations of elastic properties studied in this manuscript: (**A**) bulk modulus (*K*): measure of elastic resistance to hydrostatic compression (**B**) Young's modulus (*E*): measure of resistance in length during uniaxial tension or compression (**C**) shear modulus (*G*): measure of the resistance when subjected to opposing shear forces**.** Computational mechanical properties of non-interpenetrated NU-1200 and interpenetrated STA-26.

The bulk modulus (*K*) of a material is a measure of the elastic resistance to hydrostatic compression and related to the ratio of volumetric stress over the volumetric strain ($K = -V\,\mathrm{d}P/\mathrm{d}V$) in an isothermal process. The Young's modulus (*E*) is a measure of a material's ability to deform under uniaxial constraint (tension or compression). The Young's modulus is equivalent to the tensile stress over the tensile strain ($E = \sigma/\varepsilon$). The shear modulus ($G = Fl/A\Delta x$) is the measure of deformation of one surface of a material while an opposite face of the material experiences an opposing force. The shear modulus is the ratio of shear stress to shear strain. Our DFT results show that interpenetration nearly doubles the value of the bulk modulus and increases the Young's and shear moduli by 60%. These calculations reveal that the interpenetrated STA-26 framework is stiffer and more mechanically robust than the NU-1200 non-interpenetrated structure.

Table 1. Experimental Properties of non-interpenetrated NU-1200 and interpenetrated STA-26.

MOF	Experimental Bulk Modulus (*K*)	Experimental Young's Modulus (*E*)
NU-1200	5.7 ± 0.3 GPa	2.3 GPa
STA-26	21.1 ± 0.5 GPa	3.8 GPa

We determined the bulk modulus (K) for the NU-1200 and STA-26 MOFs using *in situ* synchrotron PXRD using a diamond anvil cell (DAC) pressure apparatus at the 17-BM beamline (λ = 0.45418 Å) at the Advanced Photon Source at Argonne National Laboratory. The PXRD peaks of the two MOFs shift to higher angles of diffraction upon the application of modest pressures, which we applied up to 0.55 GPa (**S28-S29**) and indicate compression along all crystallographic axes of the MOF sample. By first extracting the unit cell volume from the location of our diffraction features and then using a second-order Birch Murnaghan equation of state, we determine the bulk modulus of each MOF (**Fig. 5A**). The plots of the unit cell volumes vs. pressure reveal the interpenetrated STA-26 MOF has a higher bulk modulus (K = 21.1 ± 0.5 GPa) than the non-interpenetrated NU-1200 (K = 5.7 ± 0.3 GPa) (**Fig. S27**). The experimental data for the interpenetrated STA-26 MOF aligns well with the second-order model, even though the computationally derived value for the bulk modulus of the interpenetrated MOF is 6.0 GPa lower than the experimental value. The difference between the values for the bulk modulus of NU-1200 is only 2.4 GPa. However, the experimental data exhibits deviations from the best fit using a second order Birch Murnaghan equation of state (**Fig. S27**). This discontinuity at low pressures may indicate mechanically induced phase transitions.[60, 61]

Indeed, the computationally derived elastic tensors support that phase transitions may occur at low pressures in NU-1200. We found that the tetragonal shear modulus, C_{11}–C_{12}, value of NU-1200 is the lowest eigenvalue of all calculated elastic tensors for both structures, which suggests that this system is the least robust to elastic mechanical deformation and is therefore prone to phase transitions. In particular, C_{11}–C_{12} is 0.6 GPa for the non-interpenetrated NU-1200 phase, meaning the system will likely undergo a phase transition upon the application of modest amounts of pressure (**Fig. S25**). Due to the large coordination number of NU-1200, it remains mechanical stable at ambient pressure, while other highly porous MOFs with low shear moduli have been

shown to be unstable under guest removal.[62] Therefore, the tetragonal shear is the softest mode of deformation.

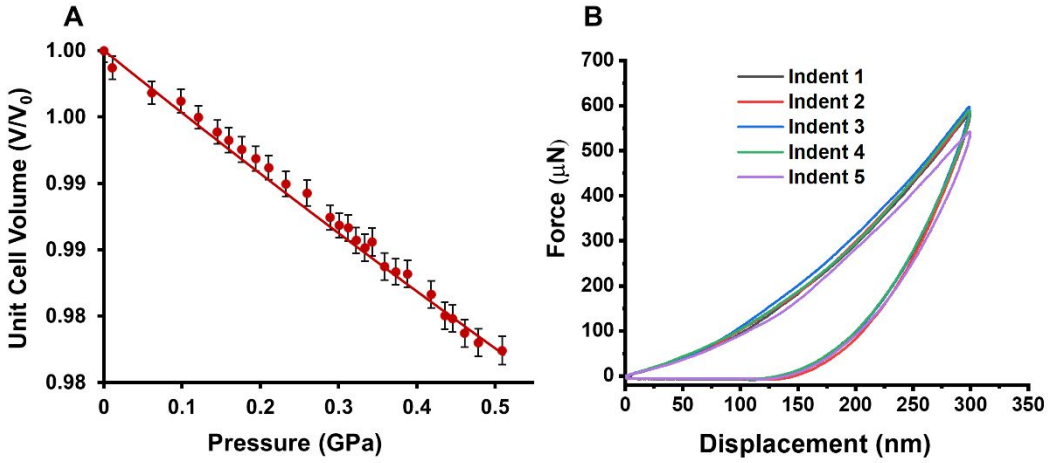

Figure 5. (**A**) Relative lattice compression of interpenetrated STA-26 obtained using *in-situ* synchrotron PXRD to determine the bulk modulus. Line represents the second-order Birch–Murnaghan equation-of-state fit to the data. (**B**) Example of Force vs Displacement curves of interpenetrated STA-26 sample obtained using single crystal nanoindentation to determine the Young's modulus.

In addition to the bulk modulus, we also determined the Young's moduli (*E*) using single crystal nanoindentation methods (**Fig 5B**). We plotted the load-displacement data **(Figure S30-S31**) from each indentation and obtained the Young's modulus and hardness as a function of indentation depth using the method proposed by Oliver and Pharr.[63] By averaging measurement over five indentations, we assign the Young's modulus of NU-1200 as 2.9 GPa with a hardness of 100 MPa and the Young's modulus of STA-26 as 4.6 GPa with a hardness of 300 MPa. These values agree well with those determined using computational methods, which also reveal that the non-interpenetrated NU-1200 is softer than the STA-26 under uniaxial compression. Collectively, our experimental and computational findings reveal that STA-26 is considerably more structurally robust than NU-1200. These findings demonstrate that interpenetrated MOFs are likely more stable to all forms of mechanical stress, including those listed here (hydrostatic, uniaxial, and shear) than their non-interpenetrated, chemically identical analogues. This indicates that if a sample includes a mixture of interpenetrated and non-interpenetrated crystals, processing conditions are limited by the less stable MOF. Moreover, this observation suggests that if you have mixed phases, they are more likely to deform under mechanical stress.

Complementary Gas Sorption of Physically Mixed MOF Systems

One potential application for MOFs is the capture and detoxification of chemical warfare agents such as a potent blistering agent, mustard gas.[64,65] Since the interpenetrated STA-26 and non-interpenetrated NU-1200 MOFs exhibit different pore structures and N_2 uptake capacities, we hypothesized that they would likely exhibit different adsorption characteristics for *n*-hexane, which we used as a structural mimic for mustard gas due to similarity in size and hydrophobicity of these two molecules.[66] The uptake trends we report can only be directly applied to *n*-hexane; however, we can use this hydrocarbon as a model to begin to understand more complex compounds, such as mustard gas. We collected *n*-hexane adsorption isotherms in both pure phase MOFs and variable mixtures of the two pure phases. We observed a much greater uptake of *n*-hexane at lower partial pressure in the interpenetrated microporous STA-26 MOF than in the mesoporous non-interpenetrated NU-1200 MOF. The 100% STA-26 sample reaches saturation at 0.01 P/P_0 while the 100% NU-1200 sample reaches saturation at 0.05 P/P_0 (**Fig. 6**). This data suggests that the interpenetrated MOF will exhibit better performance for low concentration capture of mustard gas but the non-interpenetrated NU-1200 will have an overall higher capacity for toxic gas capture. To support this observation, we plotted the total uptake of hexanes (cc g^{-1}) plotted against each sample (**Fig. S23**) and found a linear relationship (R^2= 0.98) between the two. This indicates that benefits may exist by combining different interpenetrations of MOF crystallites within a single capture device.

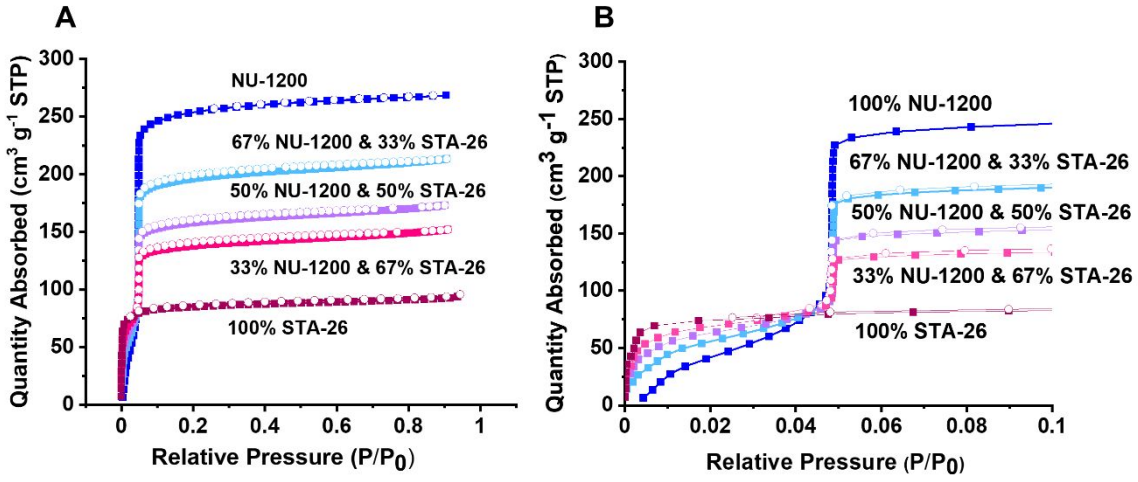

Figure 6. (**A**) *n*-hexane adsorption isotherms for physical mixture of pure-phase samples.(**B**) Blow up of 0-0.1 P/P_0 region for *n*-hexane adsorption isotherms for physical mixture of pure-phase samples.

CONCLUSIONS

In summary, we have investigated the interpenetration of the zirconium cluster-based mesoporous NU-1200 MOF to the chemically identical microporous STA-26 MOF at the bulk and single-particle limits. Using bulk methods, one may propose that we have obtained partially interpenetrated crystallites. However, we find that our X-ray diffraction, gas adsorption, and transmission electron microscopy measurements better describe our system as statistical mixtures of crystallites with integral values of interpenetration, rather than fractionally occupied phases. This suggests that interpenetration, once initialized, occurs rapidly. Experimental and computational evaluation of the mechanical properties for each framework revealed that the interpenetrated phase is more mechanically robust and thermodynamically stable than its non-interpenetrated counterpart. Finally, we find that these two phases exhibit radically different uptake behavior for *n*-hexane. Isotherms of mixed-phase systems show intermediate uptake behavior, which suggests that an opportunity exists to systematically tune adsorption characteristics by mixtures of variably interpenetrated crystallites, which we have shown can be obtained by *de novo* synthetic methods. Future studies should aim to explore mechanistic processes and physical characteristics related to interpenetrated MOFs more broadly, which we suspect will be an important area of study for the commercial deployment of these materials.

ASSOCIATED CONTENT

Supporting Information

Physical methods and instrumentation, syntheses of TMTB linker and Zr-MOFs, PXRD data, NMR data, SEM and TEM images, mapping script, computational methods, and mechanical properties measurements.

AUTHOR INFORMATION

Corresponding Authors

*E-mail: nathan.gianneschi@northwestern.edu and o-farha@northwestern.edu

Author Contributions

#L.R. and X.G. contributed equally. The manuscript was written though contributions of all authors. All authors have given approval to the final version of the manuscript.

ACKNOWLEDGEMENTS

O.K.F. gratefully acknowledges the financial support from the Air Force Research Laboratory (FA8650-15-2-5518) for the MOF materials synthesis. O.K.F. gratefully acknowledges support from the Defense Threat Reduction Agency (HDTRA1-19-1-0007) for the physical stability and sorption measurements. O.K.F. and N.C.G. gratefully acknowledge support from National Science Foundation's MRSEC program (grant number NSF DMR-1720139). N.C.G acknowledges the Army Research Office for support of the development of TEM for MOFs (W911NF-15-1-0189). M.D. acknowledges the financial support from the Inorganometallic Catalyst Design Center, an Energy Frontier Research Center funded by the U.S. Department of Energy, Office of Science, Basic Energy Sciences under award no. DE-SC0012702. F.-X.C. is supported by the Agence Nationale de la Recherche (project MATAREB, ANR-18-CE29-0009-01), and access to HPC platforms was provided by a GENCI grant (A0090807069). X.G. gratefully acknowledges the support of the Northwestern University Ryan Fellowship granted by the International Institute of Nanotechnology and The Graduate School at Northwestern University. M.C.W. and Z.H.S are supported by the NSF Graduate Research Fellowship under grant DGE-1842165. A.M.E. is supported by the NSF Graduate Research Fellowship under grant DGE-1324585. F.A.S. is supported by the Department of Defense (DoD) through the National Defense Science & Engineering Graduate (NDSEG) Fellowship Program. The authors thank Dr. Yuyang Wu and Dr. Yongbo Zhang for assistance in acquiring and interpreting the solid state NMR data reported herein. Use was made of the IMSERC X-ray facility at Northwestern University, which has received support from the Soft and Hybrid Nanotechnology Experimental (SHyNE) Resource (NSF ECCS-1542205), the State of Illinois, and the International Institute for Nanotechnology (IIN). Use was made of NMR-Hg400-solids at Northwestern University, which has received support from National Science Foundation (CHE-9871268) and International Institute for Nanotechnology (IIN).This work made use of the SPID facility of Northwestern University's NUANCE Center, which has received support from the Soft and Hybrid Nanotechnology Experimental (SHyNE) Resource (NSF ECCS-1542205); the MRSEC program (NSF DMR-1720139) at the Materials Research Center; the International Institute for Nanotechnology (IIN);

the Keck Foundation; and the State of Illinois, though the IIN. This work made use of the EPIC facility of Northwestern University's NUANCE Center, which has received support from the Soft and Hybrid Nanotechnology Experimental (SHyNE) Resource (NSF ECCS-1542205), the MRSEC program (NSF DMR-1720139) at the Materials Research Center, the International Institute for Nanotechnology (IIN), the Keck Foundation, and the State of Illinois through the IIN. This research used resources of the Advanced Photon Source, a U.S. Department of Energy (DOE) Office of Science User Facility operated for the DOE Office of Science by Argonne National Laboratory under contract no. DE-AC02- 06CH11357.

REFERENCES

1. Zhou, H. C.; Long, J. R.; Yaghi, O. M., Introduction to Metal–Organic Frameworks. *Chem. Rev.* **2012,** *112* (2), 673-674.
2. Perry Iv, J. J.; Perman, J. A.; Zaworotko, M. J., Design and synthesis of metal–organic frameworks using metal–organic polyhedra as supermolecular building blocks. *Chem. Soc. Rev.* **2009,** *38* (5), 1400-1417.
3. Howarth, A. J.; Liu, Y.; Li, P.; Li, Z.; Wang, T. C.; Hupp, J. T.; Farha, O. K., Chemical, Thermal and Mechanical Stabilities of Metal–Organic Frameworks. *Nat. Rev. Mater.* **2016,** *1* (3), 15018.
4. Yuan, S.; Qin, J.-S.; Lollar, C. T.; Zhou, H.-C., Stable Metal–Organic Frameworks with Group 4 Metals: Current Status and Trends. *ACS Cent. Sci.* **2018,** *4* (4), 440-450.
5. Bon, V.; Senkovska, I.; Weiss, M. S.; Kaskel, S., Tailoring of network dimensionality and porosity adjustment in Zr- and Hf-based MOFs. *CrystEngComm* **2013,** *15* (45), 9572-9577.
6. Jiang, H.; Zhang, W.; Kang, X.; Cao, Z.; Chen, X.; Liu, Y.; Cui, Y., Topology-Based Functionalization of Robust Chiral Zr-Based Metal–Organic Frameworks for Catalytic Enantioselective Hydrogenation. *J. Am. Chem. Soc.* **2020,** *142* (21), 9642-9652.
7. Wasson, M. C.; Buru, C. T.; Chen, Z.; Islamoglu, T.; Farha, O. K., Metal–Organic Frameworks: A Tunable Platform to Access Single-Site Heterogeneous Catalysts. *Appl. Catal., A* **2019,** *586*, 117214.
8. Wang, S.; Lee, J. S.; Wahiduzzaman, M.; Park, J.; Muschi, M.; Martineau-Corcos, C.; Tissot, A.; Cho, K. H.; Marrot, J.; Shepard, W.; Maurin, G.; Chang, J.-S.; Serre, C., A Robust Large-Pore Zirconium Carboxylate Metal–Organic Framework for Energy-Efficient Water-Sorption-Driven Refrigeration. *Nat. Energy* **2018,** *3* (11), 985-993.
9. Chen, Z.; Li, P.; Zhang, X.; Li, P.; Wasson, M. C.; Islamoglu, T.; Stoddart, J. F.; Farha, O. K., Reticular Access to Highly Porous acs-MOFs with Rigid Trigonal Prismatic Linkers for Water Sorption. *J. Am. Chem. Soc.* **2019,** *141* (7), 2900-2905.
10. Xu, W.; Yaghi, O. M., Metal–Organic Frameworks for Water Harvesting from Air, Anywhere, Anytime. *ACS Cent. Sci.* **2020,** *6* (8), 1348-1354.

11. Chen, Z.; Hanna, S. L.; Redfern, L. R.; Alezi, D.; Islamoglu, T.; Farha, O. K., Reticular chemistry in the rational synthesis of functional zirconium cluster-based MOFs. *Coord. Chem. Rev.* **2019,** *386*, 32-49.
12. Lin, R.-B.; Xiang, S.; Xing, H.; Zhou, W.; Chen, B., Exploration of porous metal–organic frameworks for gas separation and purification. *Coord. Chem. Rev.* **2019,** *378*, 87-103.
13. Batten, S. R.; Robson, R., Interpenetrating Nets: Ordered, Periodic Entanglement. *Angew. Chem. Int. Ed.* **1998,** *37* (11), 1460-1494.
14. Chen, B.; Eddaoudi, M.; Hyde, S. T.; O'Keeffe, M.; Yaghi, O. M., Interwoven Metal-Organic Framework on a Periodic Minimal Surface with Extra-Large Pores. *Science* **2001,** *291* (5506), 1021-1023.
15. Ferguson, A.; Liu, L.; Tapperwijn, S. J.; Perl, D.; Coudert, F.-X.; Van Cleuvenbergen, S.; Verbiest, T.; van der Veen, M. A.; Telfer, S. G., Controlled Partial Interpenetration in Metal–Organic Frameworks. *Nat. Chem.* **2016,** *8* (3), 250-257.
16. Fernandez, C. A.; Liu, J.; Thallapally, P. K.; Strachan, D. M., Switching Kr/Xe Selectivity with Temperature in a Metal–Organic Framework. *J. Am. Chem. Soc.* **2012,** *134* (22), 9046-9049.
17. Liang, W.; Bhatt, P. M.; Shkurenko, A.; Adil, K.; Mouchaham, G.; Aggarwal, H.; Mallick, A.; Jamal, A.; Belmabkhout, Y.; Eddaoudi, M., A Tailor-Made Interpenetrated MOF with Exceptional Carbon-Capture Performance from Flue Gas. *Chem* **2019,** *5* (4), 950-963.
18. Jiang, H.-L.; Makal, T. A.; Zhou, H.-C., Interpenetration Control in Metal–Organic Frameworks for Functional Applications. *Coord. Chem. Rev.* **2013,** *257* (15), 2232-2249.
19. Zhang, Y.; Zhang, X.; Chen, Z.; Otake, K.-i.; Peterson, G. W.; Chen, Y.; Wang, X.; Redfern, L. R.; Goswami, S.; Li, P.; Islamoglu, T.; Wang, B.; Farha, O. K., A Flexible Interpenetrated Zirconium-Based Metal–Organic Framework with High Affinity toward Ammonia. *ChemSusChem* **2020,** *13* (7), 1710-1714.
20. Xu, X.; Li, S.; Liu, Q.; Liu, Z.; Yan, W.; Zhao, L.; Zhang, W.; Zhang, L.; Deng, F.; Cong, H.; Deng, H., Isolated π-Interaction Sites in Mesoporous MOF Backbone for Repetitive and Reversible Dynamics in Water. *ACS Appl. Mater. Interfaces* **2019,** *11* (1), 973-981.
21. Duan, Z.; Li, Y.; Xiao, X.; Huang, X.; Li, X.; Li, Y.; Zhang, C.; Zhang, H.; Li, L.; Lin, Z.; Zhao, Y.; Huang, W., Interpenetrated Metal–Organic Frameworks with ftw Topology and Versatile Functions. *ACS Appl. Mater. Interfaces* **2020,** *12* (16), 18715-18722.
22. Kong, X.-J.; He, T.; Zhang, Y.-Z.; Wu, X.-Q.; Wang, S.-N.; Xu, M.-M.; Si, G.-R.; Li, J.-R., Constructing new metal–organic frameworks with complicated ligands from "One-Pot" in situ reactions. *Chem. Sci.* **2019,** *10* (14), 3949-3955.
23. Chen, D.; Xing, H.; Wang, C.; Su, Z., Highly efficient visible-light-driven CO2 reduction to formate by a new anthracene-based zirconium MOF via dual catalytic routes. *J. Mater. Chem. A* **2016,** *4* (7), 2657-2662.
24. Lippke, J.; Brosent, B.; von Zons, T.; Virmani, E.; Lilienthal, S.; Preuße, T.; Hülsmann, M.; Schneider, A. M.; Wuttke, S.; Behrens, P.; Godt, A., Expanding the Group of Porous Interpenetrated Zr-Organic Frameworks (PIZOFs) with Linkers of Different Lengths. *Inorg. Chem.* **2017,** *56* (2), 748-761.
25. Schaate, A.; Roy, P.; Preuße, T.; Lohmeier, S. J.; Godt, A.; Behrens, P., Porous Interpenetrated Zirconium–Organic Frameworks (PIZOFs): A Chemically Versatile Family of Metal–Organic Frameworks. *Chem. Eur. J.* **2011,** *17* (34), 9320-9325.
26. Cavka, J. H.; Jakobsen, S.; Olsbye, U.; Guillou, N.; Lamberti, C.; Bordiga, S.; Lillerud, K. P., A New Zirconium Inorganic Building Brick Forming Metal Organic Frameworks with Exceptional Stability. *J. Am. Chem. Soc.* **2008,** *130* (42), 13850-13851.
27. Marshall, R. J.; Griffin, S. L.; Wilson, C.; Forgan, R. S., Stereoselective Halogenation of Integral Unsaturated C-C Bonds in Chemically and Mechanically Robust Zr and Hf MOFs. *Chem. Eur. J.* **2016,** *22* (14), 4870-4877.

28. Doan, T. L. H.; Nguyen, H. L.; Pham, H. Q.; Pham-Tran, N.-N.; Le, T. N.; Cordova, K. E., Tailoring the Optical Absorption of Water-Stable ZrIV- and HfIV-Based Metal–Organic Framework Photocatalysts. *Chem. Asian J.* **2015,** *10* (12), 2660-2668.
29. Zhang, D.; Yin, Q.; Li, L.; Liu, T.-F.; Chen, Y.-P., Two interpenetrated metal-organic frameworks: The CH4 and CO2 adsorption and in-situ XRD studies. *Inorg. Chem. Commun.* **2019,** *108*, 107503.
30. Marshall, R. J.; Kalinovskyy, Y.; Griffin, S. L.; Wilson, C.; Blight, B. A.; Forgan, R. S., Functional Versatility of a Series of Zr Metal–Organic Frameworks Probed by Solid-State Photoluminescence Spectroscopy. *J. Am. Chem. Soc.* **2017,** *139* (17), 6253-6260.
31. Wang, H.; Yu, L.; Lin, Y.; Peng, J.; Teat, S. J.; Williams, L. J.; Li, J., Adsorption of Fluorocarbons and Chlorocarbons by Highly Porous and Robust Fluorinated Zirconium Metal–Organic Frameworks. *Inorg. Chem.* **2020,** *59* (7), 4167-4171.
32. Feng, L.; Yuan, S.; Qin, J.-S.; Wang, Y.; Kirchon, A.; Qiu, D.; Cheng, L.; Madrahimov, S. T.; Zhou, H.-C., Lattice Expansion and Contraction in Metal-Organic Frameworks by Sequential Linker Reinstallation. *Matter* **2019,** *1* (1), 156-167.
33. Xie, L.-H.; Liu, X.-M.; He, T.; Li, J.-R., Metal-Organic Frameworks for the Capture of Trace Aromatic Volatile Organic Compounds. *Chem* **2018,** *4* (8), 1911-1927.
34. Gao, S.; Zhao, L.; Han, L.; Zhang, Z.; Zhao, H., Synthesis, structure and characterization of two solvatochromic metal–organic frameworks for chemical-sensing applications. *CrystEngComm* **2018,** *20* (16), 2237-2240.
35. Yu, L.; Wang, H.; Liu, W.; Teat, S. J.; Li, J., Blue-Light-Excitable, Quantum Yield Enhanced, Yellow-Emitting, Zirconium-Based Metal–Organic Framework Phosphors Formed by Immobilizing Organic Chromophores. *Cryst. Growth Des.* **2019,** *19* (12), 6850-6854.
36. Kong, X.-J.; Zhang, Y.-Z.; He, T.; Wu, X.-Q.; Xu, M.-M.; Wang, S.-N.; Xie, L.-H.; Li, J.-R., Two interpenetrated metal–organic frameworks with a slim ethynyl-based ligand: designed for selective gas adsorption and structural tuning. *CrystEngComm* **2018,** *20* (39), 6018-6025.
37. Xu, L.; Luo, Y.-P.; Sun, L.; Xu, Y.; Cai, Z.-S.; Fang, M.; Yuan, R.-X.; Du, H.-B., Highly Stable Mesoporous Zirconium Porphyrinic Frameworks with Distinct Flexibility. *Chem. Eur. J.* **2016,** *22* (18), 6268-6276.
38. Chen, C.-X.; Wei, Z.-W.; Cao, C.-C.; Yin, S.-Y.; Qiu, Q.-F.; Zhu, N.-X.; Xiong, Y.-Y.; Jiang, J.-J.; Pan, M.; Su, C.-Y., All Roads Lead to Rome: Tuning the Luminescence of a Breathing Catenated Zr-MOF by Programmable Multiplexing Pathways. *Chem. Mater.* **2019,** *31* (15), 5550-5557.
39. DeCoste, J. B.; Peterson, G. W., Metal–Organic Frameworks for Air Purification of Toxic Chemicals. *Chem. Rev.* **2014,** *114* (11), 5695-5727.
40. Islamoglu, T.; Chen, Z.; Wasson, M. C.; Buru, C. T.; Kirlikovali, K. O.; Afrin, U.; Mian, M. R.; Farha, O. K., Metal–Organic Frameworks against Toxic Chemicals. *Chem. Rev.* **2020,** *120* (16), 8130-8160.
41. Liu, T.-F.; Vermeulen, N. A.; Howarth, A. J.; Li, P.; Sarjeant, A. A.; Hupp, J. T.; Farha, O. K., Adding to the Arsenal of Zirconium-Based Metal–Organic Frameworks: the Topology as a Platform for Solvent-Assisted Metal Incorporation. *Eur. J. Inorg. Chem.* **2016,** *2016* (27), 4349-4352.
42. Wang, B.; Lv, X.-L.; Feng, D.; Xie, L.-H.; Zhang, J.; Li, M.; Xie, Y.; Li, J.-R.; Zhou, H.-C., Highly Stable Zr(IV)-Based Metal–Organic Frameworks for the Detection and Removal of Antibiotics and Organic Explosives in Water. *J. Am. Chem. Soc.* **2016,** *138* (19), 6204-6216.
43. Bumstead, A. M.; Cordes, D. B.; Dawson, D. M.; Chakarova, K. K.; Mihaylov, M. Y.; Hobday, C. L.; Düren, T.; Hadjiivanov, K. I.; Slawin, A. M. Z.; Ashbrook, S. E.; Prasad, R. R. R.; Wright, P. A., Modulator-Controlled Synthesis of Microporous STA-26, an Interpenetrated 8,3-Connected Zirconium MOF with the the-i Topology, and its Reversible Lattice Shift. *Chem. Eur. J.* **2018,** *24* (23), 6115-6126.

44. We induced the interpenetration of the NU-1200 MOF by subjecting the non-interpenetrated activated framework to a solution of DMF and formic acid at 120°C. The decrease in pH due to the formic acid, along with the addition of thermal energy to the system leads to a rapid interpretation process. We posit that the process begins with the breaking of the coordination bonds between the hard acid Zr^{4+} ions and the hard base carboxylate oxygens of the tritopic TMTB linker by protonation of the linker followed by a reformation of the framework when the MOF solution was placed within the oven at 120°C. The formic acid modulator may select for the thermodynamic product (STA-26) over the kinetic product (NU-1200) by competing with the TMTB ligands for the metal ions and protons in solution, which could slow the self-assembly process. The decomposition of DMF at elevated temperatures is also well-documented within the MOF literature and produces methyl amine as the decomposition product, which can act as a base to raise the pKa of the solution and allow the free linker molecules to reform bonds to the Zr-nodes in an interpenetrated fashion.
45. Gong, X.; Gnanasekaran, K.; Chen, Z.; Robison, L.; Wasson, M. C.; Bentz, K. C.; Cohen, S. M.; Farha, O. K.; Gianneschi, N. C., Insights into the Structure and Dynamics of Metal–Organic Frameworks via Transmission Electron Microscopy. *J. Am. Chem. Soc.* **2020,** *142* (41), 17224-17235.
46. Moggach, S. A.; Bennett, T. D.; Cheetham, A. K., The Effect of Pressure on ZIF-8: Increasing Pore Size with Pressure and the Formation of a High-Pressure Phase at 1.47 GPa. *Angew. Chem. Int. Ed.* **2009,** *48* (38), 7087-7089.
47. Widmer, R. N.; Lampronti, G. I.; Chibani, S.; Wilson, C. W.; Anzellini, S.; Farsang, S.; Kleppe, A. K.; Casati, N. P. M.; MacLeod, S. G.; Redfern, S. A. T.; Coudert, F.-X.; Bennett, T. D., Rich Polymorphism of a Metal–Organic Framework in Pressure–Temperature Space. *J. Am. Chem. Soc.* **2019,** *141* (23), 9330-9337.
48. Gagnon, K. J.; Beavers, C. M.; Clearfield, A., MOFs Under Pressure: The Reversible Compression of a Single Crystal. *J. Am. Chem. Soc.* **2013,** *135* (4), 1252-1255.
49. Li, W.; Probert, M. R.; Kosa, M.; Bennett, T. D.; Thirumurugan, A.; Burwood, R. P.; Parinello, M.; Howard, J. A. K.; Cheetham, A. K., Negative Linear Compressibility of a Metal–Organic Framework. *J. Am. Chem. Soc.* **2012,** *134* (29), 11940-11943.
50. Tan, J. C.; Bennett, T. D.; Cheetham, A. K., Chemical structure, network topology, and porosity effects on the mechanical properties of Zeolitic Imidazolate Frameworks. *Proc. Natl. Acad. Sci. U. S. A.* **2010,** *107* (22), 9938-9943.
51. Redfern, L. R.; Farha, O. K., Mechanical Properties of Metal–Organic Frameworks. *Chem. Sci.* **2019,** *10* (46), 10666-10679.
52. Peterson, G. W.; DeCoste, J. B.; Glover, T. G.; Huang, Y.; Jasuja, H.; Walton, K. S., Effects of Pelletization Pressure on the Physical and Chemical Properties of the Metal–Organic Frameworks $Cu_3(BTC)_2$ and UiO-66. *Micropor. Mesopor. Mat.* **2013,** *179*, 48-53.
53. Purewal, J. J.; Liu, D.; Yang, J.; Sudik, A.; Siegel, D. J.; Maurer, S.; Müller, U., Increased Volumetric Hydrogen Uptake of MOF-5 by Powder Densification. *Int. J. Hydrog. Energy* **2012,** *37* (3), 2723-2727.
54. Kitao, T.; Zhang, Y.; Kitagawa, S.; Wang, B.; Uemura, T., Hybridization of MOFs and polymers. *Chem. Soc. Rev.* **2017,** *46* (11), 3108-3133.
55. Evans, J. D.; Fraux, G.; Gaillac, R.; Kohen, D.; Trousselet, F.; Vanson, J.-M.; Coudert, F.-X., Computational Chemistry Methods for Nanoporous Materials. *Chem. Mater.* **2017,** *29* (1), 199-212.
56. Le, S.-N.; Navrotsky, A., Energetics of formation of alkali and ammonium cobalt and zinc phosphate frameworks. *J. Solid State Chem.* **2008,** *181* (1), 20-29.
57. Trofymluk, O.; Levchenko, A. A.; Tolbert, S. H.; Navrotsky, A., Energetics of Mesoporous Silica: Investigation into Pore Size and Symmetry. *Chem. Mater.* **2005,** *17* (14), 3772-3783.
58. Hughes, J. T.; Bennett, T. D.; Cheetham, A. K.; Navrotsky, A., Thermochemistry of Zeolitic Imidazolate Frameworks of Varying Porosity. *J. Am. Chem. Soc.* **2013,** *135* (2), 598-601.

59. Bennett, T. D.; Simoncic, P.; Moggach, S. A.; Gozzo, F.; Macchi, P.; Keen, D. A.; Tan, J.-C.; Cheetham, A. K., Reversible pressure-induced amorphization of a zeolitic imidazolate framework (ZIF-4). *ChemComm* **2011,** *47* (28), 7983-7985.
60. Widmer, R. N.; Lampronti, G. I.; Anzellini, S.; Gaillac, R.; Farsang, S.; Zhou, C.; Belenguer, A. M.; Wilson, C. W.; Palmer, H.; Kleppe, A. K.; Wharmby, M. T.; Yu, X.; Cohen, S. M.; Telfer, S. G.; Redfern, S. A. T.; Coudert, F.-X.; MacLeod, S. G.; Bennett, T. D., Pressure Promoted Low-Temperature Melting of Metal–Organic Frameworks. *Nat. Mater.* **2019,** *18* (4), 370-376.
61. Chapman, K. W.; Halder, G. J.; Chupas, P. J., Pressure-Induced Amorphization and Porosity Modification in a Metal−Organic Framework. *J. Am. Chem. Soc.* **2009,** *131* (48), 17546-17547.
62. Yan, Y.; Juríček, M.; Coudert, F.-X.; Vermeulen, N. A.; Grunder, S.; Dailly, A.; Lewis, W.; Blake, A. J.; Stoddart, J. F.; Schröder, M., Non-Interpenetrated Metal–Organic Frameworks Based on Copper(II) Paddlewheel and Oligoparaxylene-Isophthalate Linkers: Synthesis, Structure, and Gas Adsorption. *J. Am. Chem. Soc.* **2016,** *138* (10), 3371-3381.
63. Oliver, W. C.; Pharr, G. M., Measurement of Hardness and Elastic Modulus by Instrumented Indentation: Advances in Understanding and Refinements to Methodology. *J. Mater. Res.* **2004,** *19* (1), 3-20.
64. Bobbitt, N. S.; Mendonca, M. L.; Howarth, A. J.; Islamoglu, T.; Hupp, J. T.; Farha, O. K.; Snurr, R. Q., Metal–organic Frameworks for The Removal of Toxic Industrial Chemicals and Chemical Warfare Agents. *Chem. Soc. Rev.* **2017,** *46* (11), 3357-3385.
65. Son, F. A.; Wasson, M. C.; Islamoglu, T.; Chen, Z.; Gong, X.; Hanna, S. L.; Lyu, J.; Wang, X.; Idrees, K. B.; Mahle, J. J.; Peterson, G. W.; Farha, O. K., Uncovering the Role of Metal–Organic Framework Topology on the Capture and Reactivity of Chemical Warfare Agents. *Chem. Mater.* **2020,** *32* (11), 4609-4617.
66. Chen, H.; Snurr, R. Q., Understanding the Loading Dependence of Adsorbate Diffusivities in Hierarchical Metal–Organic Frameworks. *Langmuir* **2020,** *36* (5), 1372-1378.

Table of Contents Figure